Materials Advances

ROYAL SOCIETY OF CHEMISTRY

PAPER

View Article Online
View Journal

Cite this: DOI: 10.1039/d6ma00301j

Luminous nematic threads: single-component liquid crystals self-assemble into fluorescent fibers

D. Megha, [a] B. Venugopal, [a] Anjali Ganjiwale, [b] H. T. Srinivasa, [c] Arun Roy [c] and G. Shanker *[a]

Received 5th March 2026,
Accepted 28th March 2026

DOI: 10.1039/d6ma00301j

rsc.li/materials-advances

We report the synthesis and mesomorphic behaviour of two new series of liquid crystal dimers derived from *N*-alkylation of 1,4-phenylenedimethanamine with 4-cyanobiphenyl units linked by aliphatic spacers (n = 4–10). Polarizing optical microscopy, differential scanning calorimetry and X-ray diffraction show that most dimers display nematic phases, with several exhibiting stable supercooled mesophases at room temperature. In thick films, rare ±1 nematic defects drive the spontaneous formation of fluorescent fibers (quantum yield 72.1%), with Schlieren patterns revealing local variations in elasticity and viscosity. This molecular design offers insights into self-assembling luminous nematic fibers for optoelectronic applications.

1. Introduction

Liquid crystals represent a captivating class of stimuli-responsive soft materials, including colloids, gels, and biomaterials. They show pronounced responses to external stimuli, like electric fields, temperature, magnetic fields, light, and chemical environment, rendering them ideal for optoelectronic applications such as LEDs, photovoltaics, optical fibers, laser diodes, and photoresistors.[1–3] This state of matter is thermodynamically stable, uniquely blending the directional order of crystals with the fluidity of liquids. Their facile alignment along specific directions and rapid reorientation render them highly suitable for commercial applications.[4] In 1972, George W. Gray introduced cyanobiphenyl liquid crystals, a breakthrough that propelled liquid-crystal display (LCD) technology and revolutionized the field. These compounds exhibit low or room-temperature mesophases, serving as cornerstones for LC applications owing to their broad mesophase ranges, synthetic accessibility, high yields, large positive dielectric anisotropy, strong birefringence, and chemical stability. Rod-shaped monomers such as 5CB and 8CB display room-temperature nematic phases, driven by high polarizability and the electron-withdrawing terminal cyano group.[5–8] The terminal cyano group enhances dipolar interactions, stabilizing the nematic phase. Among LCs, dimers outshine monomers and trimers through superior mesophase stability and dynamic responsiveness. Their spacer-induced bent conformations enable diverse, often rare phases including twist bend nematic, re-entrant nematic, and heliconal cholesteric with tunable thermal and optical properties.[9–12] Fluorescence based liquid crystals yield powerful, tunable, multifunctional optical materials, with promise for luminescent solar concentrators, organic light emitting diodes (OLEDs), and organic semiconductors. Combining self-assembly with fluorescence affords superior properties, such as efficient packing and defined emission over random polymeric or dye-doped systems.[13,14]

Tailored functional moieties and molecular designs invariably yield compelling results, from fundamental insights to applications. Numerous reports highlight secondary amide based LCs, including discotic variants with amides fused to ring structures.[15–17] *N*-Methyl amides as linkers for chiral aliphatic tails on aromatic cores,[18,19] and mesogens with *N*,*N*-dialkyl amide terminals have been reported.[20] Most mesogens feature phenyl rings linked by short unsaturated ester or imine groups. In contrast, secondary and tertiary amine linkages remain rare in low-molar-mass liquid crystals, despite their key structural roles in technologically vital liquid crystalline polymers.[15–17] Valeria Nori *et al.* synthesized *N*-alkylated amide derivatives, including diarylamines, *N*-methylphenylamines, and carbazoles from aryl esters using 10 mol% $B(C_6F_5)_3$ catalyst, and no mesomorphic phase was reported.[21] Notably, no reports exist on the liquid crystalline properties of *N*-alkylated benzyl diamines, representing a major gap. We introduce the first such derivatives exhibiting mesophases, including room-temperature variants. Integrating this *N*-alkylated benzyl diamine core into tailored mesogenic architectures

[a] Department of Chemistry, Bangalore University, Jnana Bharathi Campus, Bengaluru 560056, India. E-mail: maanshanker@gmail.com
[b] Department of Life Sciences, Bangalore University, Jnana Bharathi Campus, Bangalore, 560056, India
[c] Raman Research Institute, Soft Condensed Matter Group, C. V. Raman Avenue, Sadashivanagara, Bengaluru, 560080, India

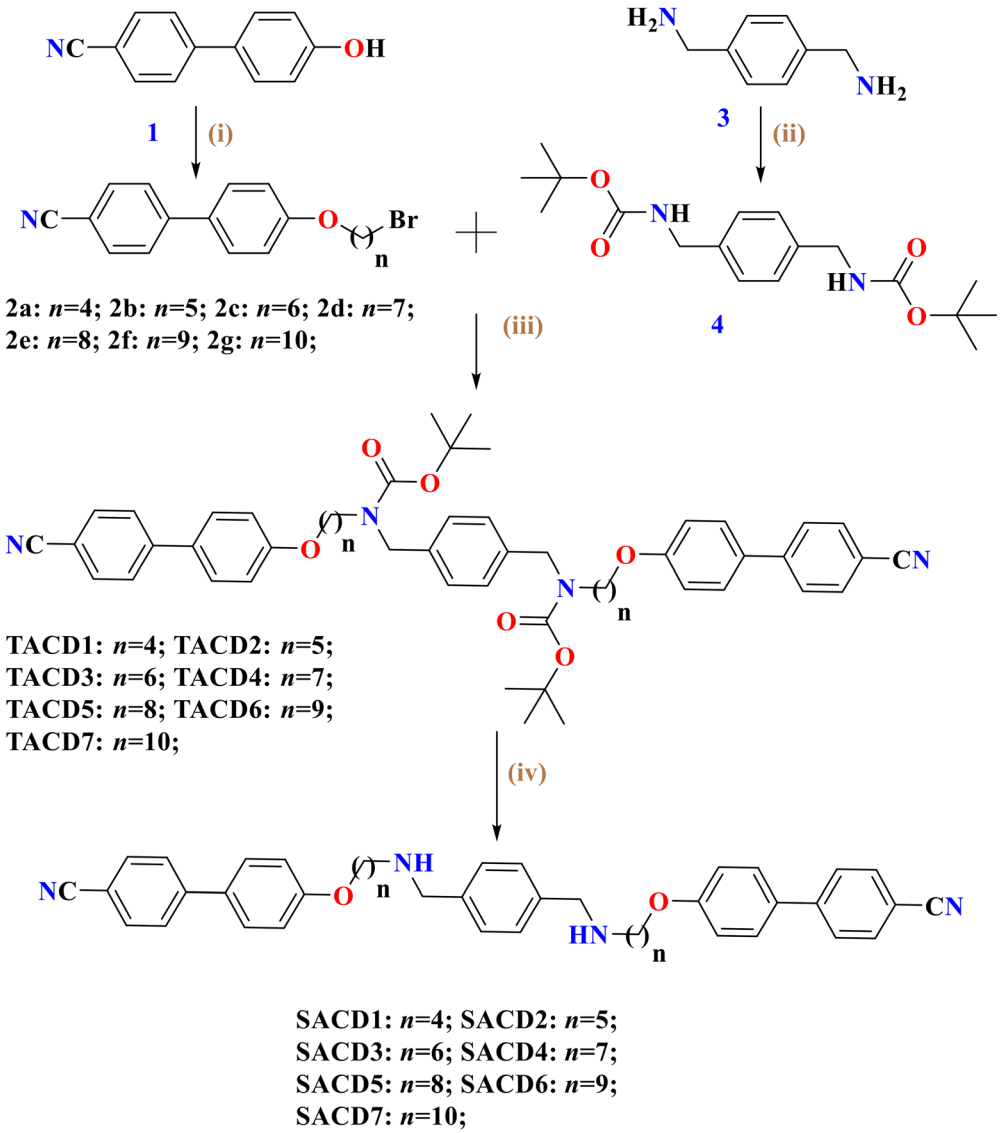

Scheme 1 Synthesis of dimers **TACD*n*** and **SACD*n***; Reagents and conditions: (i) Dibromoalkanes, K_2CO_3, Butanone, RT, 16 h, under N_2, (85–87%); (ii) Boc anhydride, H_2O, 50 °C, 6 h, under N_2, (quantitative %); (iii) KO^{t}Bu, dry DMF, 0 °C to RT, 8 h, under N_2, (59–63%); (iv) Hydrogen chloride, 4 M in 1,4-dioxane, DCM, RT, 4 h, under N_2, (58–62%).

holds strong promise for advanced optoelectronic and display applications.

Mantosh K. Sinha *et al.* prepared *N*-alkylated benzyl diamines with aliphatic/aromatic chains to form stopper free pseudorotaxanes, but no LC properties were reported.[22] Strachan *et al.* synthesized secondary/tertiary *N*-methyl benzanilide-based mesogens. The secondary amides exhibit nematic phases, including the first reported twist bend nematic phase for amides.[23]

We report novel *N*-alkylated 1,4-phenylenedimethanamine dimers with 4-cyano-4′-(*n*-bromoalkane-1-yloxy)biphenyl spacers (n = 4–10). Tertiary amine **TACD*n*** shows low melting/room-temperature nematics; secondary **SACD*n*** shows nematics. **TACD3** forms ~240 mm long fluorescent nematic fibers that remain stable at room temperature when suspended, without rupturing *via* Rayleigh–Plateau instability up to an hour, and exhibit strong fluorescence throughout.[7]

2. Experimental section

2.1. Materials and methods

The starting materials, 4-cyano-4′-hydroxybiphenyl, 1,4-phenylenedimethanamine and dibromoalkane spacers, were sourced from Sigma-Aldrich and used without purification. Solvents were dried conventionally; products were purified by silica gel (100–200 mesh) column chromatography (hexane/ethyl acetate). Structures were confirmed by ^{1}H and ^{13}C NMR (Bruker AMX-400, 400/100 MHz). Phase transitions were determined *via* Mettler Toledo DSC (peaks in °C, ΔH in kJ mol^{-1}), and mesophases identified on a Leica DM2700P POM with a Linkam HS-420 hot stage. XRD was performed on a Panalytical Empyrean (Cu Kα, 1.54 Å), CHN analysis on a Leco CHNS-932,UV-Vis (chloroform, 200-1100 nm, concentration-dependent) on a GENESYS 50, and emission measurements on a Shimadzu RF-6000.

2.2. Molecular design and synthesis

TACD*n* and **SACD*n*** dimers were synthesized as in Scheme 1, with intermediates **2a-g** and **4** synthesized from reported methods.[24,25] Intermediates **2a-g** were synthesized *via* Williamson etherification of 4-cyano-4′-hydroxybiphenyl with dibromoalkane spacers (see SI). *N*-alkylation of compound **4** with **2a-g** (KO^{t}Bu) afforded **TACD*n***; subsequent deprotection yielded **SACD*n*** in good yields. Detailed synthetic procedures, analytical data, NMR, and IR profiles are in the SI (Fig. S1–S3).

3. Results and discussion

3.1. Thermal and mesomorphic behavior

The thermal and mesomorphic behaviours of **TACD*n*** and **SACD*n*** were probed by DSC and POM, with XRD performed on representative compounds from both series. DSC quantified the transition enthalpies as shown (Table 1 and Fig. 1). Among the **TACD*n*** series, several compounds (**TACD2**, **TACD4**, **TACD5**, **TACD6**) failed to exhibit liquid crystalline phases (Fig. 1a), likely owing to the *tert*-butoxycarbonyl substituent on the nitrogen. This lateral group disrupts the rod-like molecular architecture essential for mesophase formation. It also lowers the melting temperature, as seen in comparisons with the deprotected **SACD*n*** dimers. Exceptions include **TACD1** and **TACD3**, which display nematic phases, while the longest homologue, **TACD7**, shows a grainy phase emerging from the crystals at 4.34 °C (ΔH = 1.3 kJ mol^{-1}), clearing to isotropic at 123.7 °C (ΔH = 2.4 kJ mol^{-1}). Cooling reveals reversible Iso-X at 123.5 °C (ΔH = −2.5 kJ mol^{-1}), with a super-cooled nature below room temperature (Fig. 1b and Table 1). Upon heating from the crystalline state, the molecules transition to a grainy texture of higher order Smectic *via* melting, and the rigid cyanobiphenyl rods with polar –CN termini self-assemble into layered domains, with the polar groups at one end, as the molecules line up side by side. This tight packing creates stable higher order smectic layers, like neat stacks of rods, where smectic slabs form through dipole-enhanced lateral packing. Long **TACD7** spacers confer flexibility, nucleating independent grains rather than uniform layers where each grain represents a coherent block of tilted molecules aligned normal to the layer plane. Grain boundaries arise from misaligned domains accommodating local curvature. Cooling from isotropic (123.5 °C) triggers layer nucleation: rod-like cores align parallel within fluid layers (∼3–4 nm spacing), inferred from CB dimers 3, with –CN dipoles locking head-to-tail. Flexible spacers bend slightly, enabling layer undulations; ether links reduce packing energy barriers. The grains grow competitively, bound by low-angle tilt walls (∼5–15°), yielding the characteristic ''grainy'' contrast as birefringent domains scatter light differently. Texture formation arises from linear cyanobiphenyl termini: strong –CN dipoles drive intermolecular associations, stabilizing grain formation in **TACD7** *via* polar packing. Long spacers and ether links impart conformational flexibility, suppressing crystal nucleation and enabling low-temperature mesophases; carbamates broaden stability, while di-*tert*-butoxy carbonyl groups increase the core free volume, further disfavoring crystallization (Fig. S4a).

All **SACD*n*** dimers exhibit liquid-crystalline (LC) phases with pronounced super-cooling nematic phase, as the linear cyanobiphenyl cores self-assemble into nematic phases through strong –CN dipole attractions ($\mu \approx$ 4–5 D)[26] and π–π stacking, favoring parallel alignment along a common director. Flexible spacers enable hairpin conformations, shortening the end-to-end distance by 20–30% and stabilizing nematicity *via* chain–chain van der Waals contacts; ether links boost entropy while tertiary amines reduce rotational barriers around the central phenylenedimethanamine, yielding high-viscosity fluids. Cyanobiphenyl π–π* emission ($\lambda_{max} \approx$ 350–400 nm) sharpens in ordered phases, as nematic alignment suppresses non-radiative decay ($\varphi \approx$ 0.2–0.4) *via* rigidified rotations. **SACD1** transitions Iso-N at 96.5 °C, and the dimers **SACD3/4** supercool; **SACD2/6/7** are enantiotropic (shown in Fig. S4b). **SACD5** spans a broad nematic range (47.7 °C to −3.7 °C), ideal for optical modulators, tunable films, and LC elastomers (LCE).[27,28]

In nematic liquid crystals (Fig. 2a), four-fold Schlieren brushes arise from disclinations where the director aligns

Table 1 Phase transition temperature (°C) and associated enthalpies (ΔH kJ mol^{-1})[a] for the **TACD*n*** and **SACD*n*** series

Phase sequence		
Dimers	2nd heating	1st cooling
TACD1	Cr 21.38 [1.2] N 99.0 [0.24] Iso	Iso 93.80 [−1.6] N 46.3 [−0.2] Cr
TACD2	Cr 5.0 [1.5] Iso	Iso 4.2 [−2.1] Cr
TACD3	Cr 30.4 [51.8] N 129.9 [1.6] Iso	Iso 90.9 [−1.6] N^b
TACD4	Cr 9.46 [1.5] Iso	Iso 8.4 [−1.1] Cr
TACD5	Cr 16.4 [1.2] Iso	Iso 15.36 [−1.4] Cr
TACD6	Cr 5.9 [1.02] Iso	Iso 5.7 [−1.05] Cr
TACD7	Cr 4.34 [1.3] X^c 123.7 [2.4] Iso	Iso 123.5 [−2.2] X^c
SACD1	Cr 55.8 [16.7] N 73.7 [0.17] Iso	Iso 96.5 N*30.5 [−2.1] Cr
SACD2	Cr 61.5 [1.79] N 91.73 [6.6] Iso	Iso 73.5 [−2.44] N 0.8 [−0.5] Cr
SACD3	Cr 70.2 [2.6] N 90.5 [1.8] Iso	Iso 88.6 [−1.6] N^b
SACD4	Cr 48.8 [1.4] N 86.2 [3.6] Iso	Iso 85.9 [−5.6] N^b
SACD5	Cr 47.3 [5.76] N 72.7 [4.51] Iso	Iso 67.7 [−0.82] N −3.7 [−0.7] Cr
SACD6	Cr 61.7 [2.57] N 78.8 [0.5] Iso	Iso 86.3 [−8.1] N 61.9 [−5.3] Cr
SACD7	Cr 70.9 [6.4] N 8 103.9 [1.6] Iso	Iso 101.4 [−1.2] N 58.5 [−21.2] Cr

[a] Phase transition temperatures are determined for the 2nd heating and 1st cooling cycles from DSC measurements (10 °C min^{-1}). Cr = crystal, N = nematic, N^b freezes in nematic phase, X^c = grainy texture with sharp edges and low birefringence, Iso = isotropic, *POM observation.

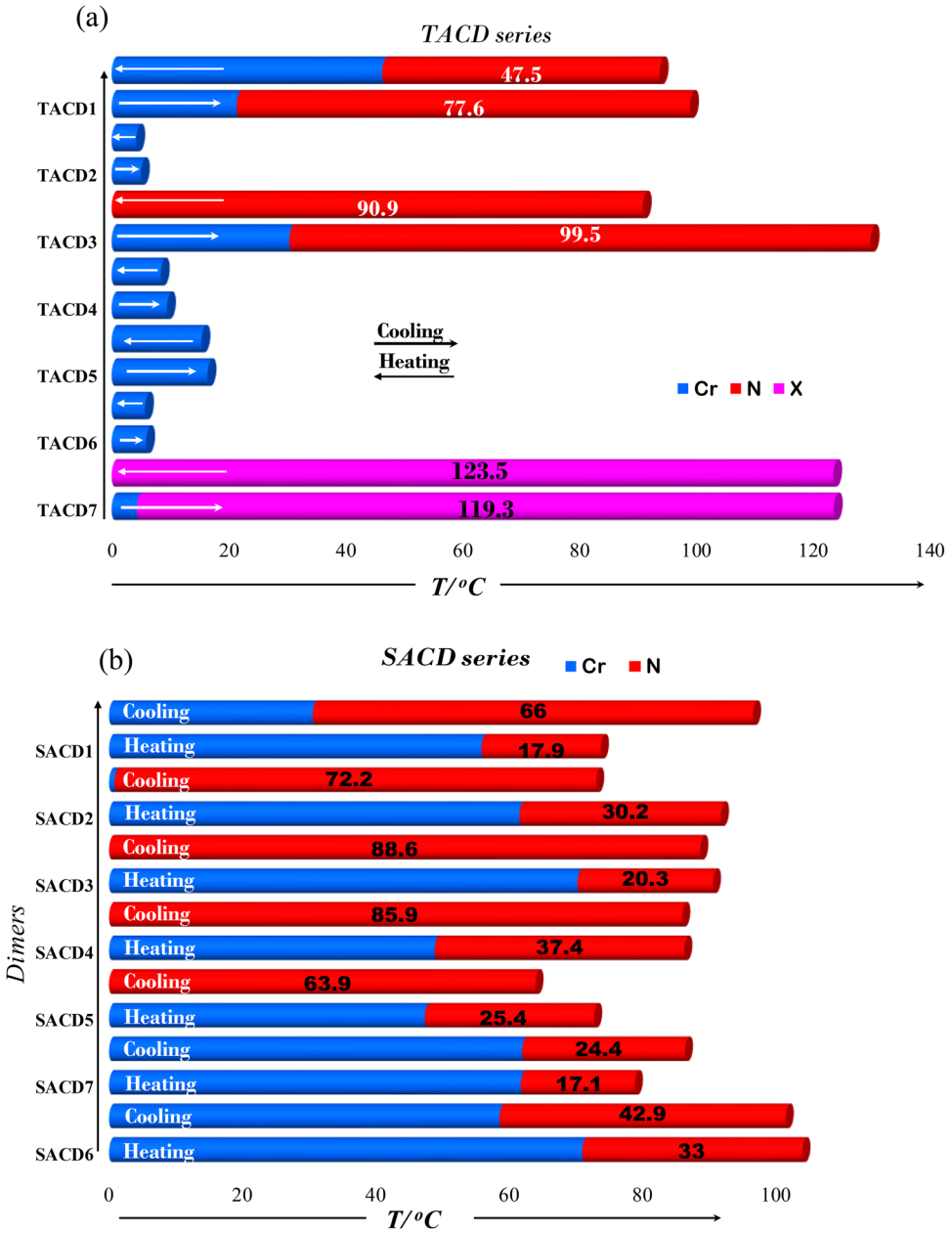

Fig. 1 Bar graph showing the LC phases and their transition temperatures of (a) **TACD*n*** and (b) **SACD*n*** in both the cycles scanned at the rate of 10 °C min^{-1}.

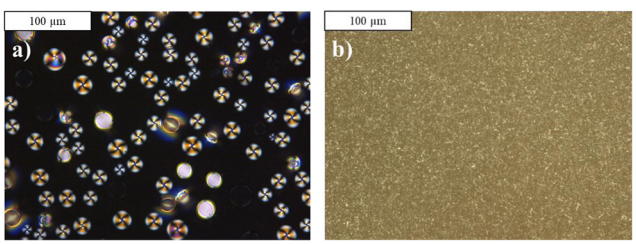

Fig. 2 POM textures of the (a) Schlieren nematic texture with four-fold brushes of strength $s = \pm 1$ of **SACD6** at 90.8 °C in cooling cycle. (b) grainy texture (X) with granular domains, sharp edges, and low birefringence of **TACD7** at 60 °C observed in the cooling cycle.

parallel or perpendicular to crossed polarizers, extinguishing transmission at 90° intervals. For ±1/2 defects, stage rotation drives brushes oppositely (counter-clockwise for +1/2, clockwise for −1/2), revealing handedness; half-integer order proves director polarity. Higher-strength $|s| = \pm 1$ defects are rarer in LC thin films due to elevated elastic energy, which drives instability into ±1/2 pairs. These defects exhibit stationary or symmetrically rotating brushes arising from full ±360° director winding and are stabilized in thicker samples or under stress. In a four-fold brush defect $s = \pm 1$, exactly four dark brushes converge at one point, reflecting the director's complete 360° rotations twice the 180° twist of two-brush $s = \pm 1/2$ defects. Brush dynamics probe elasticity and viscosity near transitions,

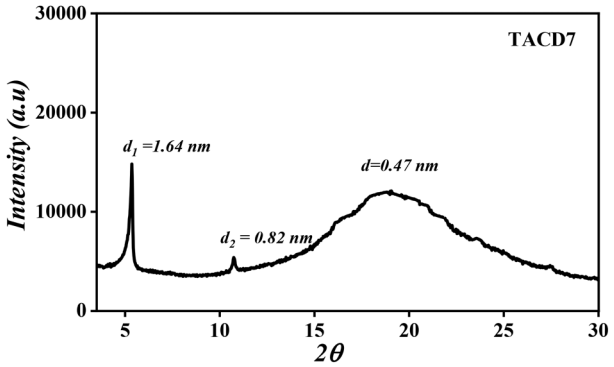

Fig. 3 SAXS and WAXS 1D plots at 30 °C of **TACD7** and molecular length calculated using steepest descent energy minimization with MMFF94 L_{mol} = 3.27 nm.

suggesting utility in light-responsive liquid crystal elastomer (LCE) actuators; **TADC7** shows granular domains (Fig. 2b) with sharp edges and low birefringence from a distorted director during cooling.[29]

3.2. XRD investigations

For further investigation of the LC phase, XRD diffraction measurements were performed on the dimer **TACD7**. The figure illustrates the X-ray analysis of SAXS and WAXS of the **TACD7** obtained at 30 °C (Fig. 3), where a sharp peak is observed at the small-angle region with a *d*-spacing value of d_1 = 1.64 nm and d_2 = 0.82 nm, and a broad hump with a *d*-spacing value of 0.47 m indicates the liquid like ordering. The molecule exhibits a d/L_{mol} ratio of 0.625, which indicates an intercalated arrangement of molecules within the grainy texture, where the distorted director forms individual grains that are intercalated and comparable in size to the molecular length L_{mol} (3.27 nm), and are not prominently resolved (Fig. 2b).

4. Fluorescent freely suspended fibers

TACD3 uniquely forms freely suspended fibers that extend to ~240 mm in length and ~0.2–0.4 mm in diameter without rupturing, drawn by needle pulling at room temperature (25 °C; Fig. 4). These fibers remain stable for up to an hour before rupturing due to Rayleigh-Plateau instability, fragmenting into droplets to minimize surface energy.[30] Polarized optical microscopy reveals nematic droplets within the fiber at 68 °C,[7] and such fiber formation common in non-Newtonian fluids like liquid crystals typically arises from the liquid phase, solidifying into a glassy state.[30–32] Highly fluorescent **TACD3** yields emissive fibers upon elongation (Fig. 4c and d). Although discotic liquid crystals with one-dimensional columnar order or smectic C phases readily stabilize fibers *via* layered or columnar structures, nematic phases are less prone to this owing to the absence of positional order and susceptibility to Plateau–Rayleigh instability. Here, **5CB** units in the nematic phase of **TACD3** aggregate *via* dipolar interactions, forming a dynamic network that imparts non-Newtonian behavior. This creates long-range order along the director, and it keeps fluidity but adds anisotropic surface tension. This favors stable, elongated fibers over round droplets, which thin and break over time as the surface energy relaxes lower.[33] Low-viscosity **TACD3** makes 240 mm luminous fibers *via* nematic instability. Tension gradients and splay flow stretch them, with elasticity (K11 ≈ 5-pN) holding until they break.[8,34–36]

5. Aggregational studies

UV-visible spectroscopy of **TACDn** and **SACDn** (Fig. 5) dimers in chloroform revealed similar absorption profiles across concentrations, irrespective of Boc protection in **TACDn**. Two bands dominate: n → π* (235–256 nm, heteroatom-induced) and π → π* (250–346 nm). Intensity drops and peaks broaden with higher concentration, showing *H*-aggregation. This happens due to –CN group dipoles, van der Waals forces, and tight packing around the biphenyl core. The electronegative –CN narrows the band gap *via* charge transfer, stabilizing nematic phases. Polymethylene spacers—$(CH_2)_n$—decouple the cores: odd-parity yields bent, blue-shifted conformations; even-parity, linear, red-shifted ones. Longer spacers enhance π-delocalization, reducing the band gaps and tuning the mesophase behavior.[37] Aliphatic spacers—$(CH_2)_n$—dictate aggregation in bulk and solution phases, enabling intramolecular folding and intermolecular π-stacking that yield excimers, aggregation-induced quenching (AIQ) or emission (AIE). UV-visible spectra (Fig. 5) show aggregation *via* band broadening from excitonic coupling and scattering most pronounced in longer-spacer systems with tighter packing. Spacer length tunes liquid crystal anisotropy: shorter chains rigidify structures,

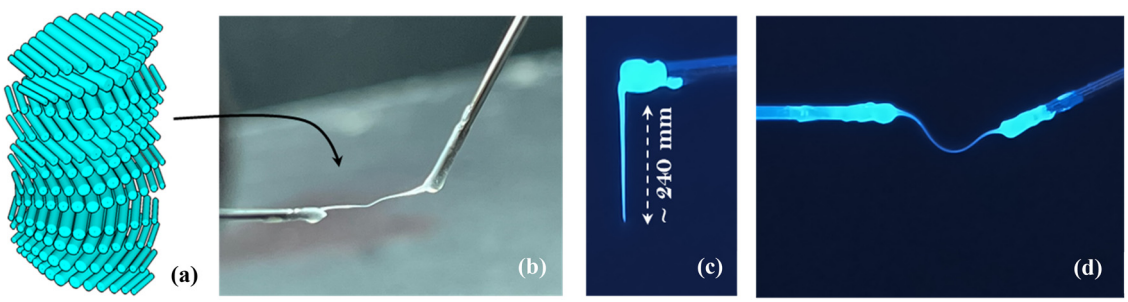

Fig. 4 (a) Self-assembly of nematogens, (b) fiber formation, and (c) and (d) fluorescent nematic thread of ~240 mm of **TACD3** at 25 °C upon excitation.

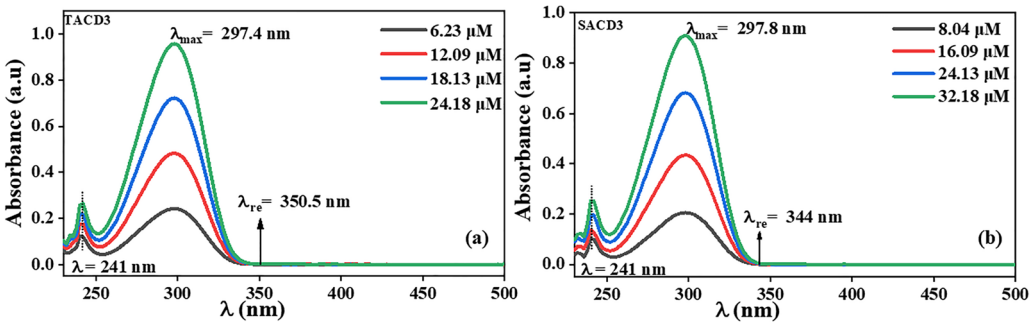

Fig. 5 Absorption spectra of **TACD3** (a) and **SACD3** (b) in chloroform as a function of concentration (for others, see the SI, Fig. S5).

boosting orientational order, birefringence, dielectric anisotropy and refractive index dispersion through enhanced cyano-dipole coupling. This favours low-voltage switching *via* stronger dipolar alignment under electric fields. Longer spacers increase flexibility, diminishing these properties.[38,39]

UV-visible absorption spectroscopy and Planck's equation measure the HOMO–LUMO energy gap using the following equation:

$$E = h\nu = \frac{hc}{(\text{red edge})} = 1243\ \text{nm}\frac{\text{eV}}{(\text{red edge})} \qquad (1)$$

where $C = 2.998 \times 10^8\ \text{ms}^{-1}$, $h = 6.636 \times 10^{-34}$ Js is Planck's constant and λ is the absorption onset wavelength. As shown in Fig. 5, the estimated energy gap from the red edge wavelength using eqn (1) is shown in Table 2.[40]

Among the two series, **TACDn** molecules show less energy gap than **SACDn**, and the *tert*-butoxycarbonyl (Boc) group converts a non-conjugated amine lone pair into a conjugated carbamate system. This stabilizes molecular orbitals and lowers the HOMO–LUMO energy gap compared to the unprotected amine.

6. Emission spectra

Photoluminescence spectra (Fig. 6) reveal intense S_1-state emissions for **TACD*n*** and **SACD*n*** dimers, with Stokes shifts linking emission to UV-visible absorption onsets. Each shows dual peaks: a high-intensity B band ($\sim\lambda_{em1}$ 356 nm) and lower-intensity Q bands ($\sim\lambda_{em2}$ 718 nm). **SACD*n*** outperforms **TACD*n*** due to steric hindrance curbing non-radiative decay *via* restricted rotations and vibrations.[27] **TACD3** (a) and **SACD3** (b) exhibit robust emission (356–720 nm) upon 296 nm excitation. Optimal planarity, packing and flexibility at $n = 6$ minimize aggregation-caused quenching (ACQ): the biphenyl core stays planar, the spacer provides steric stability, and nematic phases enhance alignment. Shorter chains ($n < 6$) boost π–π stacking and non-radiative paths; longer ones ($n > 6$) introduce excessive flexibility and rotations. This $n = 6$ spot also optimizes charge distribution and orbital overlap, maximizing radiative efficiency.[41,42]

Table 2 Experimentally determined energy gap from the red edge wavelength

Dimers	$\lambda_{(\text{red edge})}$ (nm)	E (eV)
TACD1	351	3.53
TACD2	351	3.53
TACD3	351	3.54
TACD4	351	3.53
TACD5	351	3.53
TACD6	351	3.53
TACD7	351	3.53
SACD1	346	3.58
SACD2	345	3.59
SACD3	345	3.59
SACD4	345	3.59
SACD5	345	3.59
SACD6	346	3.58
SACD7	345	3.59

High-energy (short-wavelength) B-band emission arises from rapid (nanoseconds) $S_1 \rightarrow S_0$ transitions in locally excited (LE) states or stable exciplexes, typical of rigid π-conjugated biphenyls.[43] Low-energy Q bands reflect intermolecular excimers or aggregates, enhanced by π–π stacking and excitonic coupling. In chloroform, rising concentration promotes *J*-aggregates *via* solvent-driven self-assembly, boosting dimer emission while minimizing background, ideal for micro-environmental sensing or bio-imaging. The Q-band intensity is ~25% of the B band, indicating preferential *J* over *H*-aggregate formation; further studies are needed at fixed concentrations. Cyano-biphenyl dimers show strong solution-phase fluorescence under UV, with a 58 nm Stokes shift enabling clean spectral separation *via* filters. Solvent-mediated aggregation and excitonic coupling drive excited-state dynamics and emission red shifts.[44] The fluorescent quantum yield was calculated for the **TACD6** and **SACD6** by the optical dilution method using anthracene in ethanol as a reference (quantum yield/Φ_s = 0.27) by using eqn (2).[45]

$$\Phi_u = [(A_s F_u n^2)/(A_u F_s n_o^2)]\Phi_s \qquad (2)$$

where 'u' refers to the unknown and 's' to the standard. Φ represents the quantum yield, A is the absorbance at the excitation wavelength, F denotes the integrated emission area across the band, and 'n' are the indices of refraction of the solvent containing the unknown (compound) and the standard (n_o) at the sodium D line, respectively. The temperature of the emission measurement is also recorded. The D line is employed, assuming minimal dispersion among standard solvents. A quantum yield of 0.335 and 0.721 is obtained for the **TACD6** and **SACD6**, respectively. A high fluorescence quantum yield (%) of 72.1% for **SACD6** marks exceptional performance,

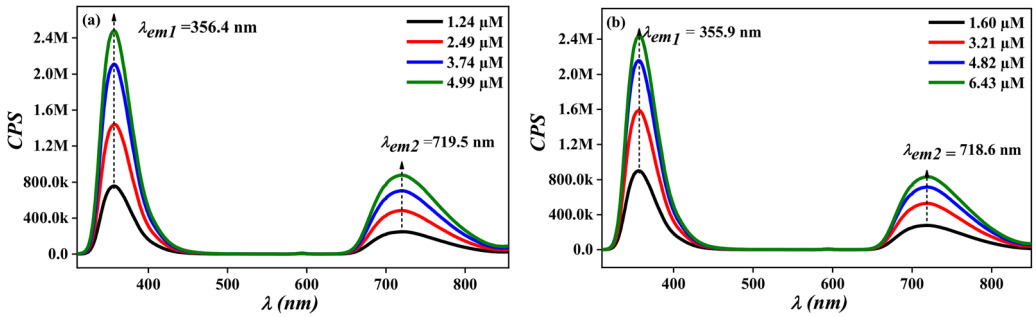

Fig. 6 Emission spectra of **TACD3** (a) and **SACD3** (b) in chloroform as a function of concentration (for others, see the SI, Fig. S6).

rivalling commercial dyes and ideal for high-luminous nematic fiber applications.[46–48]

Conclusions

These *N*-alkylated cyanobiphenyl dimers provide stable nematic phases near room temperature that spontaneously form fluorescent fibers with quantum yields up to 72.1% (**SACD6**). In thick films, rare ±1 nematic defects stabilized by high order and viscosity drive this self-assembly, with Schlieren patterns mapping local elasticity and viscosity. This design enables dipolar cyanobiphenyls to sustain supercooled states for light-responsive actuators, luminescent solar concentrators and adaptive sensors, bridging molecular engineering with soft-matter optoelectronics.

Author contributions

D. Megha: synthesis, investigation, and formal analysis. B. Venugopal: methodology, investigation, and formal analysis. Anjali Ganjiwale: methodology, investigation, and formal analysis. H. T. Srinivasa, and Arun Roy: validation, methodology, and investigation. G. Shanker: writing original draft, writing review and editing, validation, supervision, and conceptualization.

Conflicts of interest

The authors declare that they have no known competing financial interests or personal relationships that could have appeared to influence the work reported in this paper.

Data availability

Supplementary information (SI): all synthesis procedures, NMR, IR, MS spectra, and XRD data. See DOI: https://doi.org/10.1039/d6ma00301j.

Liquid crystal data, DSC/POM/XRD, are provided in the main text. No new primary data are required.

Acknowledgements

Dr G. Shanker and Anjali Ganjiwale acknowledge the financial support from the Anusandhan National Research Foundation under the Partnerships for Accelerated Innovation and Research (PAIR) scheme (Project No. ANRF/PAIR/2025/000021/PAIR-A) for carrying out this research work, and UGC-FRP. Megha D thanks KSTePS, DST, Government of Karnataka, for the PhD Fellowship financial support. Vasudha K. N., Technical Officer C, Soft Condensed Matter Laboratory, Raman Research Institute, Bengaluru, India, is also gratefully acknowledged for her support and assistance.

References

1 R. J. Bushby and K. Kawata, Liquid crystals that affected the world: discotic liquid crystals, *Liq. Cryst.*, 2011, **38**, 1415–1426.
2 J. A. Castellano, *Liquid gold: the story of liquid crystal displays and the creation of an industry*, World Scientific, 2005.
3 G. Shanker, K. S. Kumar and B. Paul, Perspective on structure-property relationship of room temperature single component liquid crystals, *Liq. Cryst.*, 2022, **49**, 1545–1603.
4 H. K. Bisoyi and Q. Li, Liquid crystals: versatile self-organized smart soft materials, *Chem. Rev.*, 2021, **122**, 4887–4926.
5 G. W. Gray, *Handbook of liquid crystals, Vol. 2B: low molecular weight liquid crystals II, Mol. Cryst.*, 1969, **7**, 127–151.
6 A. Ožegović, J. Hobbs, R. Mandle, A. Lesac and A. Knežević, Chiral cyanobiphenyl dimers–significance of the linking group for mesomorphic properties and helical induction, *J. Mater. Chem. C*, 2024, **12**, 13985–13993.
7 M. K. Srinatha, S. Poppe, G. Shanker, M. Alaasar and C. Tschierske, 2,3,4-Trihydroxy benzonitrile-based liquid crystals: fiber forming room temperature nematic phases, *J. Mol. Liq.*, 2020, **317**, 114244.
8 B. S. Ranjitha, M. Alassar and G. Shanker, Luminous and fluorescent cyanobiphenyls exhibiting super-cooled nematic phases, *Liq. Cryst.*, 2024, **51**, 1553–1564.
9 N. Trbojevic, D. J. Read and M. Nagaraj, Dielectric properties of liquid crystalline dimer mixtures exhibiting the nematic and twist-bend nematic phases, *Phys. Rev. E*, 2017, **96**, 052703.
10 C. T. Imrie and P. A. Henderson, Liquid crystal dimers and oligomers, *Curr. Opin. Colloid Interface Sci.*, 2002, **7**, 298–311.
11 P. A. Henderson and C. T. Imrie, Methylene-linked liquid crystal dimers and the twist-bend nematic phase, *Liq. Cryst.*, 2011, **38**, 1407–1414.

12 G. R. Luckhurst and G. W. Gray, *The molecular physics of liquid crystals*, Academic Press, London, 1979.
13 N. Wang, W. Bi, Y. Liu, S. Xu, K. Wang and S. Cao, Recent progress of fluorescent liquid crystals, *J. Mol. Liq.*, 2025, 127741.
14 H. Feng, Y. He, W. Yang, S. Wang and Y. S. Feng, A novel strategy for constructing fluorescent liquid crystals with diphenylacrylonitrile group derivatives based on thiazolo[5,4-*d*]thiazole core, *J. Mol. Struct.*, 2023, **1274**, 134582.
15 B. Glettner, S. Hein, R. A. Reddy, U. Baumeister and C. Tschierske, Cyclic ureas as novel building blocks for bent-core liquid crystals, *Chem. Commun.*, 2007, 2596–2598.
16 U. Stebani, G. Lattermann, R. Festag, M. Wittenberg and J. H. Wendorff, A novel class of mesogens: liquid-crystalline derivatives of linear oligoalkylene amides, *J. Mater. Chem.*, 1995, **5**, 2247–2251.
17 J. A. Duro, G. de la Torre, J. Barberá, J. L. Serrano and T. Torres, Synthesis and liquid-crystal behavior of metal-free and metal-containing phthalocyanines substituted with long-chain amide groups, *Chem. Mater.*, 1996, **8**, 1061–1066.
18 S. L. Wu and F. D. Chen, Novel chiral swallow-tailed amide liquid crystals possessing antiferroelectricity, *Liq. Cryst.*, 2003, **30**, 991–995.
19 S. Wu, Z. Yang and L. Yu, Antiferroelectric liquid crystals with amide linking group positioned at chiral tail, *Liq. Cryst.*, 2007, **34**, 1145–1149.
20 D. Pociecha, J. Szydlowska, J. Gasowska, D. Kardas, J. Mieczkowski and W. Tlaczala, New mesogenic compounds having fork-like or cyclic amide terminal groups, *Liq. Cryst.*, 2002, **29**, 663–667.
21 V. Nori, A. Dasgupta, R. Babaahmadi, A. Carlone, A. Ariafard and R. L. Melen, Triarylborane catalysed *N*-alkylation of amines with aryl esters, *Catal. Sci. Technol.*, 2020, **10**, 7523–7530.
22 M. K. Sinha, O. Reany, M. Yefet, M. Botoshansky and E. Keinan, Bistable cucurbituril rotaxanes without stoppers, *Chem. – Eur. J.*, 2012, **18**, 5589–5605.
23 G. J. Trachan, W. T. Harrison, J. M. Storey and C. T. Imrie, Understanding the remarkable difference in liquid crystal behaviour between secondary and tertiary amides: the synthesis and characterisation of new benzanilide-based liquid crystal dimers, *Phys. Chem. Chem. Phys.*, 2021, **23**, 12600–12611.
24 S. T. Wu and D. K. Yang, *Reflective liquid crystal displays*, John Wiley & Sons, 2001.
25 Y. Feliachi, A. Roy, Y. Ren, M. G. Finn and R. P. Lively, Solid-state crosslinking of thin film composite membranes for organic solvent reverse osmosis separations, *J. Membr. Sci.*, 2024, **695**, 122462.
26 M. C. López Iglesias and M. Barón, Liquid crystal birefringence and electric dipole moment relationship with temperature, weak magnetic field and molecular geometry, *J. Mol. Liq.*, 1989, **44**, 63–71.
27 S. Laschat, A. Baro, N. Steinke, F. Giesselmann, C. Hägele, G. Scalia and M. Tosoni, Discotic liquid crystals: from tailor-made synthesis to plastic electronics, *Angew. Chem., Int. Ed.*, 2007, **46**, 4832–4887.
28 C. Tschierske, Liquid crystal engineering–new complex mesophase structures and their relations to polymer morphologies, nanoscale patterning and crystal engineering, *Chem. Soc. Rev.*, 2007, **36**, 1930–1970.
29 O. D. Lavrentovich, Design of nematic liquid crystals to control microscale dynamics, *Liq. Cryst. Rev.*, 2021, **8**, 59–129.
30 A. Eremin, U. Kornek, S. Stern, R. Stannarius, F. Araoka, H. Takezoe and A. Jákli, Pattern-stabilized decorated polar liquid-crystal fibers, *Phys. Rev. Lett.*, 2012, **109**, 017801.
31 L. Rayleigh, On the instability of jets, *Proc. London Math. Soc.*, 1878, **1**, 4–13.
32 A. Nemeș, A. Eremin, R. Stannarius, M. Schulz, H. Nádasi and W. Weissflog, Structure characterization of free-standing filaments drawn in the liquid crystal state, *Phys. Chem. Chem. Phys.*, 2006, **8**, 469–476.
33 S. S. Bhattacharyya and Y. Galerne, Elongation of discotic liquid crystal strands and lubricant effects, *ChemPhysChem.*, 2014, **15**, 1432–1446.
34 Y. Arakawa, K. Komatsu, T. Shiba and H. Tsuji, Methylene- and thioether-linked cyanobiphenyl-based liquid crystal dimers CBnSCB exhibiting room temperature twist-bend nematic phases and glasses, *Mater. Adv.*, 2021, **2**, 1760–1773.
35 A. Ferrarini, G. R. Luckhurst, P. L. Nordio and S. J. Roskilly, Prediction of the transitional properties of liquid crystal dimers: a molecular field calculation based on the surface tensor parametrization, *J. Chem. Phys.*, 1994, **100**, 1460–1469.
36 C. E. Fairhurst, S. Fuller, J. Gray, M. C. Holmes and G. J. T. Tiddy, *Handbook of liquid crystals*, Wiley-VCH, New York, 1998, p. 341.
37 M. K. Srinatha, A. Zeba, A. Ganjiwale, A. Gowda, G. Hegde, M. Alaasar and G. Shanker, The influences of lateral groups on 4-cyanobiphenyl-benzonitrile-based dimers, *Liq. Cryst.*, 2022, **49**, 217–229.
38 E. Cruickshank, G. J. Strachan, K. Thapa, D. Pociecha, M. Salamończyk, J. M. Storey and C. T. Imrie, Cyanobiphenyl-based liquid crystal dimers and the twist-bend nematic phase: on the role played by the length and parity of the spacer, *Liq. Cryst.*, 2024, **51**, 1446–1470.
39 A. Kocot, M. Czarnecka, Y. Arakawa and K. Merkel, Dielectric study of liquid crystal dimers: probing the orientational order and molecular interactions in nematic and twist-bend nematic phases, *J. Phys. Chem. B*, 2023, **127**, 7082–7090.
40 A. S. Bhadwal, R. M. Tripathi, R. K. Gupta, N. Kumar, R. P. Singh and A. Shrivastav, Biogenic synthesis and photocatalytic activity of CdS nanoparticles, *RSC Adv.*, 2014, **4**, 9484–9490.
41 S. A. Oladepo, Temperature-dependent fluorescence emission of 4-cyano-4′-pentylbiphenyl and 4-cyano-4′-hexylbiphenyl liquid crystals and their bulk phase transitions, *J. Mol. Liq.*, 2021, **323**, 114590.
42 A. Kumar, A. K. Srivastava, D. Sharma, S. N. Tiwari and N. Misra, BO_2-substituted novel alkyl biphenyl liquid crystalline series: dependence of geometrical and electronic

properties on the alkyl chain length, *Theor. Chem. Acc.*, 2023, **142**, 17.

43 M. Fernández, L. López-Gandul, R. Gómez and L. Sánchez, Supramolecular polymerization of biphenyl-cyanostilbenes: triggering circularly polarized luminescence by self-assembly, *Org. Lett.*, 2025, **27**, 6561–6565.

44 J. H. Krech and S. L. Rose-Pehrsson, Effect of chlorinated hydrocarbons on the fluorescence emission spectra of 1,3-bis-(1-pyrene)propane in solutions and poly(vinyl alcohol) films, *Appl. Spectrosc.*, 1996, **50**, 1528–1534.

45 D. F. Eaton, Reference materials for fluorescence measurement, *Pure Appl. Chem.*, 1988, **60**, 1107–1114.

46 B. He, Q. Zhong, Q. Dong, X. Yang, S. J. Cowling, W. Qiao and Y. Wang, Liquid-crystalline circularly polarised TADF emitters for high-efficiency, solution-processable organic light-emitting diodes, *Mater. Horiz.*, 2024, **11**, 1251–1260.

47 R. Takkar, V. Sharma, P. Dhairwal and P. Kumar, Review of quantum dots and nanoparticles-dispersed nematic liquid crystals: electro-optical and dielectric properties, *J. Mater. Sci.: Mater. Electron.*, 2025, **36**, 310.

48 A. F. Suleymanova, J. R. Fortwengler, X. Chen, R. Czerwieniec, Y. Wang, M. Z. Shafikov and D. W. Bruce, Liquid-crystalline dual fluorescent dyes for white light emission, *J. Mater. Chem. C*, 2025, **13**, 12348–12364.